

VEMamba: Efficient Isotropic Reconstruction of Volume Electron Microscopy with Axial-Lateral Consistent Mamba

Longmi Gao Pan Gao*

College of Artificial Intelligence, Nanjing University of Aeronautics and Astronautics
Nanjing 211106, China

gaolongmi@nuaa.edu.cn, Pan.Gao@nuaa.edu.cn

Abstract

Volume Electron Microscopy (VEM) is crucial for 3D tissue imaging but often produces anisotropic data with poor axial resolution, hindering visualization and downstream analysis. Existing methods for isotropic reconstruction often suffer from neglecting abundant axial information and employing simple downsampling to simulate anisotropic data. To address these limitations, we propose VEMamba, an efficient framework for isotropic reconstruction. The core of VEMamba is a novel **3D Dependency Reordering** paradigm, implemented via two key components: an Axial-Lateral Chunking Selective Scan Module (ALCSSM), which intelligently re-maps complex 3D spatial dependencies (both axial and lateral) into optimized 1D sequences for efficient Mamba-based modeling, explicitly enforcing axial-lateral consistency; and a Dynamic Weights Aggregation Module (DWAM) to adaptively aggregate these re-ordered sequence outputs for enhanced representational power. Furthermore, we introduce a realistic degradation simulation and then leverage Momentum Contrast (MoCo) to integrate this degradation-aware knowledge into the network for superior reconstruction. Extensive experiments on both simulated and real-world anisotropic VEM datasets demonstrate that VEMamba achieves highly competitive performance across various metrics while maintaining a lower computational footprint. The source code is available on GitHub: <https://github.com/I2-Multimedia-Lab/VEMamba>

1. Introduction

Volume Electron Microscopy is a pivotal technology in modern life sciences [1, 25], medicine [3, 18, 26], and clinical diagnosis [31, 32, 34], enabling the direct 3D visualization of cellular [35, 40, 41] and tissue [29, 39] ultrastructures at nanometer resolution. Isotropic high-resolution

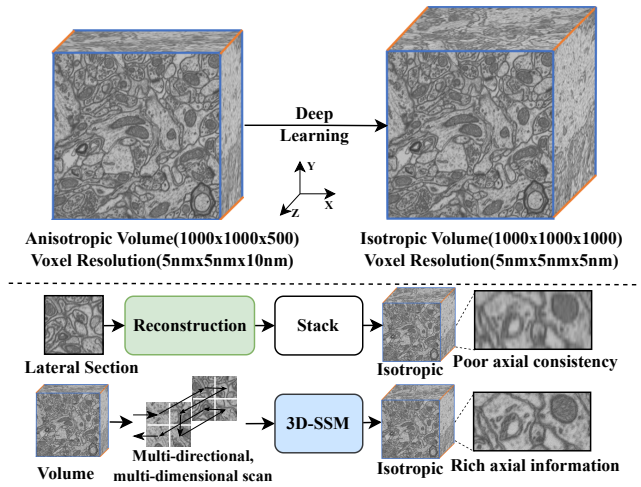


Figure 1. At the top is the Deep Learning for Isotropic Reconstruction. Compared with isotropic techniques, anisotropic techniques produce fewer axial pixels when imaging the same tissue. Deep learning is then used to compensate for the missing axial pixels. At the bottom is the Comparison between the common method and VEMamba. The common method takes lateral sections as input and reconstructs a volume by stacking, leading to poor axial consistency. In contrast, VEMamba takes volumetric input and performs multi-directional, multi-dimensional scanning, yielding rich axial information.

data are crucial for the accurate analysis and comprehensive understanding of complex biological specimens. However, most VEM imaging techniques, such as serial section Transmission Electron Microscopy (ssTEM), inherently produce anisotropic volumes [24]. These volumes suffer from lower axial (z) resolution compared to the lateral (x, y) resolution, a limitation imposed by the physical constraints of serial sectioning, as shown in Figure 1. While certain advanced techniques such as focused ion beam scanning electron microscopy (FIB-SEM) can acquire isotropic data, they suffer from prohibitively slow imaging speeds and high costs, making them impractical for widespread

*Corresponding author.

adoption [13]. Therefore, developing efficient algorithms for isotropic reconstruction from anisotropic data is essential for advancing biological research.

Early supervised method [17] showed potential, but the difficulty in obtaining isotropic data led to a shift towards self-supervised frameworks. The standard self-supervised paradigm involves training on the high-resolution lateral sections and validating the reconstruction performance on the axial dimension. However, existing self-supervised frameworks, including GAN-based [4, 12] and Diffusion-based [21, 27], still encounter fundamental limitations. First, the vast majority rely on 2D model architectures. This architectural choice prevents them from effectively modeling the 3D spatial dependency inherent in volumetric data, often leading to artifacts and a lack of coherence between adjacent slices, as shown in Figure 1. While some 3D approaches using Transformers [15, 36] have been explored, they often incur prohibitive computational costs and memory footprints, making them intractable for high-resolution volumetric data. Second, the common simulation practice of simple downsampling fails to capture the complex degradations present in real-world acquisitions. This discrepancy leads to suboptimal performance when models are deployed on real anisotropic data.

The recent advent of State Space Models [9, 10, 33], particularly the Mamba [8] architecture, presents a new opportunity to overcome these challenges. Mamba is distinguished by its ability to model global dependencies, while maintaining linear complexity and high memory efficiency [11, 22]. This unique combination makes it exceptionally well-suited for modeling large-scale 3D volume. *To the best of our knowledge, we are the first to apply the Mamba architecture for VEM isotropic reconstruction.*

Building on these advantages, we introduce VEMamba, a novel, *efficient yet effective* framework for VEM isotropic reconstruction. The core of our VEMamba architecture is composed of two components: the Axial-Lateral Chunking Selective Scan Module (ALCSSM) and the Dynamic Weights Aggregation Module (DWAM). ALCSSM is the core method for achieving 3D dependency reordering. It reorders and maps the physically separated axial (inter-slice) and lateral (intra-slice) dependencies in a 3D volume into 1D sequences that Mamba can process. By performing orthogonal axial-lateral scans, the SSM operating on these 1D sequences is forced to model both inter-slice and intra-slice information flow simultaneously, thereby explicitly establishing axial-lateral consistency. This process is further enhanced by the DWAM, which adaptively computes dynamic weights for the feature sequences generated by the different scans, enabling a more powerful and context-aware aggregation of the 3D representation. Furthermore, we introduce a degradation model incorporating multiple types of degradation including blur, downsampling, and noise to more ac-

curately simulate real anisotropic data characteristics and employ MoCo [16] for self-supervised extraction of degradation information, enabling better reconstruction of lateral sections. Our contributions can be summarized as follows:

- We propose the Axial-Lateral Chunking Selective Scan Module and Dynamic Weights Aggregation Module to implement an efficient 3D dependency reordering paradigm, ensuring robust axial-lateral consistency.
- We introduce a degradation learning framework that incorporates multiple types of degradation to accurately simulate real anisotropic data, coupled with MoCo-based self-supervised degradation extraction for enhanced lateral section reconstruction.
- Experiments demonstrate highly competitive performance on both synthetic and real VEM datasets, achieving superior reconstruction quality in the majority of evaluated settings while maintaining computational efficiency.

2. Related Work

Isotropic Reconstruction for VEM. Classical interpolation algorithms, such as bicubic or spline interpolation, offer a fast, training-free solution but often yield suboptimal and blurry results, failing to recover fine structural details.

To alleviate this issue, deep learning-based methods have become prevalent. Generative Adversarial Networks (GANs) were widely explored, leveraging the high-resolution lateral sections as an unpaired supervisory signal to restore the low-resolution axial sections [4, 12]. While promising, these GAN-based approaches are often plagued by training instability and can introduce undesirable artifacts. More recent works have explored advanced network architectures. Transformer-based models, for instance, have shown great potential. A2I-3DEM [19] integrates a Vision Transformer (ViT) with a U-Net to effectively capture multi-scale local and global image dependencies. Similarly, IsoVEM [15] employs a combination of attention mechanisms within a U-Net architecture to efficiently model intersection relationships. Inspired by advancements in video processing, some methods [6, 38] reframe the problem as video frame interpolation, though they are often limited in their reconstruction factor. Recently, diffusion models [21, 23, 27] have emerged as a powerful alternative, demonstrating superior generation quality and training stability compared to GANs. These methods typically train a model on 2D lateral slices and apply it to restore axial slices during the iterative sampling process.

Despite this progress, current methods are still hampered by the two primary challenges discussed in the Introduction: a prevalent reliance on 2D architectures that ignore 3D continuity, and simplistic degradation simulations that create a domain gap. Furthermore, each architecture class presents its own practical challenges: GANs suffer from unstable

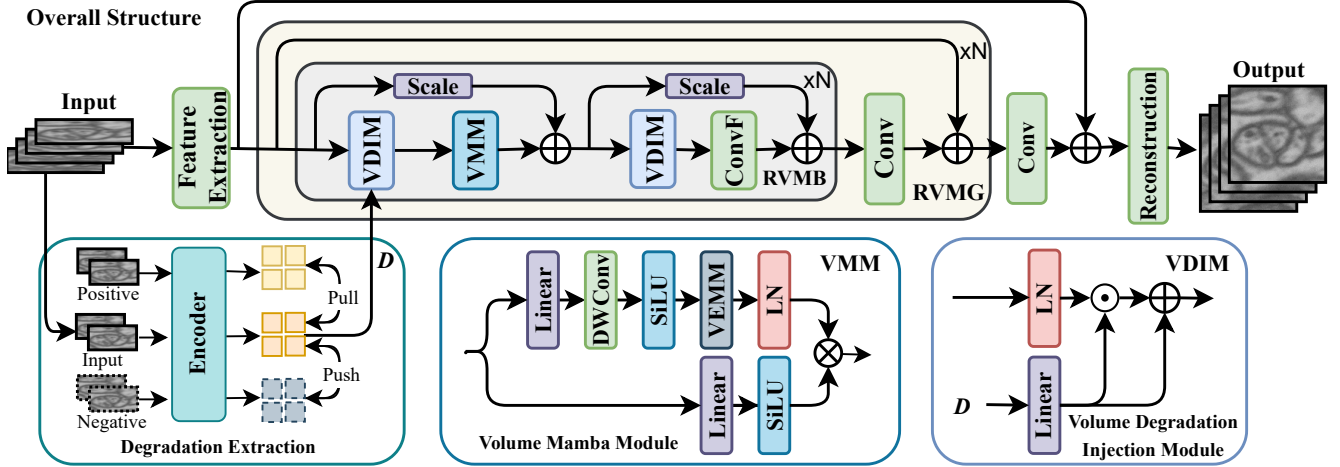


Figure 2. Visualization of VEMamba. At the top is the overall structure of VEMamba, which is primarily composed of the Residual Volume Mamba Group (RVMG), and the RVMG consists mainly of the Residual Volume Mamba Block (RVMB). On the bottom left is the Degradation Extraction. On the bottom middle is the Volume Mamba Module (VMM). On the bottom right is the Volume Degradation Injection Module (VDIM).

training, Transformers incur a prohibitive memory footprint and computational cost for large volumes, and diffusion models are notoriously slow and resource-intensive due to their iterative sampling process. Our work is designed to directly address these gaps by introducing a 3D-native, efficient Mamba-based architecture and a more realistic self-supervised framework built upon degradation modeling.

3. Method

3.1. Motivation

Our method addresses two primary challenges in VEM isotropic reconstruction.

Axial-Lateral Consistency. The key challenge is the severe anisotropy. Existing 2D methods cannot capture long-range dependencies along the axial dimension. By contrast, full 3D methods model axial dependencies but incur prohibitive computational and memory costs. This motivated us to design the VEMamba Module (VEMM), which performs 3D spatial context modeling with linear computational complexity and explicitly enforces axial-lateral consistency, thereby resolving the fundamental trade-off between 2D and 3D approaches. At its core, the ALCSSM creates a seamless flow of information across all spatial dimensions, and the DWAM adaptively fuses these multi-directional representations.

Realistic Degradation Modeling. The second challenge is the simulation gap. Common strategies using simple downsampling fail to capture the complex, real-world degradations inherent in VEM acquisition. This discrepancy limits model robustness. To address this, we introduce a more realistic degradation framework and leverage

Momentum Contrast. This allows the network to learn a degradation-aware representation in a self-supervised manner, which is then injected via the VDIM to enhance robustness and achieve a more faithful reconstruction.

3.2. Overall Architecture

Our model is composed of four main stages: a shallow feature extraction stage, a degradation extraction stage, a deep feature extraction stage, and a final reconstruction stage. The overall pipeline is illustrated in Figure 2. Specifically, the input is a single-channel anisotropic subvolume $X \in \mathbb{R}^{F \times h \times W}$, where F , h , and W represent the number of lateral sections, the height, and the width. Our goal is to reconstruct an isotropic volume $Y \in \mathbb{R}^{F \times H \times W}$, where $H = s \times h$ and s is the axial upscaling factor. Initially, the input volume X is processed by the shallow feature extraction stage to obtain shallow features $F_S \in \mathbb{R}^{F \times C \times h \times W}$, where C denotes the channel dimension of the hidden features. In parallel, the degradation extraction stage uses momentum contrast to obtain a degradation representation $D \in \mathbb{R}^L$. The shallow features F_S and the degradation representation D are then fed into the deep feature extraction stage to produce deep features $F_D \in \mathbb{R}^{F \times C \times h \times W}$. This stage is constructed by stacking several Residual Volume Mamba Groups (RVMGs), each containing multiple Residual Volume Mamba Blocks (RVMBs). A RVMB integrates three key components: a Volume Mamba Module (VMM) for capturing global context, a ConvFFN [37] (ConvF) for local details, and a Volume Degradation Injection Module (VDIM) to inject the degradation representation D . Finally, the reconstruction stage fuses the feature maps via addition ($F_S + F_D$) and upscales the result using a pixel-shuffle layer

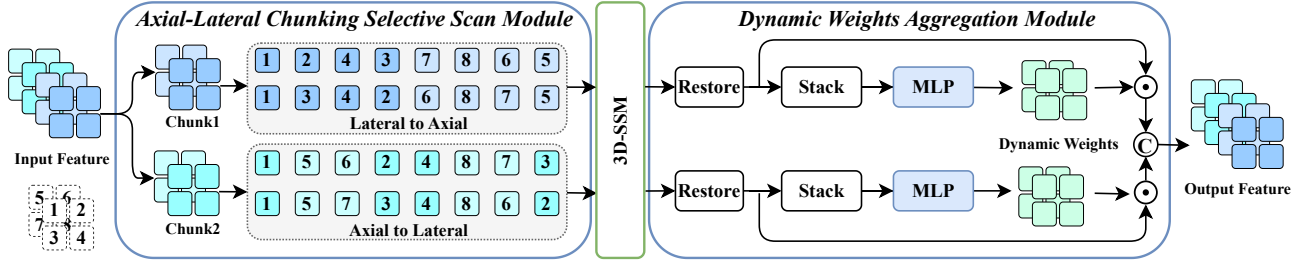


Figure 3. Visualization of the VEMamba Module (VEMM). It includes our proposed Axial-Lateral Chunking Selective Scan Module (ALCSSM), Dynamic Weights Aggregation Module (DWAM) and SSM.

followed by a convolution to produce the final output Y .

We optimize the network (except the degradation extraction stage) with a hybrid loss function combining L1 and SSIM losses:

$$\mathcal{L}_{\text{total}} = \mathcal{L}_1(Y, \hat{Y}) + \mathcal{L}_{\text{SSIM}}(Y, \hat{Y}) \quad (1)$$

where \hat{Y} is the ground-truth high-resolution volume, and Y is the reconstructed volume.

3.3. VEMamba Module

The core of VEMamba lies in the VEMamba Module (VEMM). As illustrated in Figure 3, the VEMM operates in three sequential stages: (1) it begins by partitioning the 3D feature map and employing the ALCSSM to transform these partitions into one-dimensional sequences; (2) these sequences are then processed by a SSM to capture long-range dependencies and establish a global receptive field; (3) finally, the resulting sequences are dynamically integrated using our proposed DWAM, ensuring an adaptive and context-aware fusion of multi-directional information.

ALCSSM: The ALCSSM is designed to systematically deconstruct and sequentialize the 3D feature maps in a manner that preserves the crucial interplay between axial and lateral information. This module guarantees a consistent and comprehensive representation of the volumetric data for the subsequent SSM processing. Inspired by the computational efficiency demonstrated in MobileMamba [14], we initially partition the 3D feature tensor into two distinct chunks along the channel dimension. This strategy not only reduces the GPU memory footprint but also enhances parallel processing capabilities. Subsequently, we introduce a multi-directional, multi-dimensional scanning strategy for each chunk, motivated by the continuous information flow concept in SCST [30]. As depicted in Figure 3, we employ a series of continuous 3D scanning paths that traverse the volume from “Axial-to-Lateral” and “Lateral-to-Axial.” It is crucial to note that this encompasses not only the two primary directions shown but also their reverse counterparts. This comprehensive set of eight scanning trajectories (four for each chunk) ensures a fluid and uninterrupted flow of

information across all spatial dimensions. This synergistic combination of channel partitioning and multi-directional scanning allows ALCSSM to achieve exceptional performance with high computational efficiency, rendering it well suited for the demands of VEM isotropic reconstruction.

DWAM: Following the global modeling by the SSM, the DWAM is designed to adaptively fuse the sequences generated from the diverse scanning directions. This module is critical for synthesizing the complementary information captured by each scan, thereby enabling a more robust and holistic representation of the 3D volume. As illustrated in Figure 3, let the set of eight 1D sequences processed by the SSM be denoted as $\{x_i\}_{i=1}^8$. The fusion process commences by first restoring these sequences to their original 3D spatial arrangement, F_1 and F_2 , corresponding to the two initial chunks:

$$\begin{aligned} F_1 &= \text{Restore}(\{x_i\}_{i=1}^4) \\ F_2 &= \text{Restore}(\{x_i\}_{i=5}^8) \end{aligned} \quad (2)$$

These aggregated feature tensors are stacked to form two distinct 3D feature tensors and then passed through an MLP to generate context-dependent weights, W_1 and W_2 . These weights dynamically modulate the importance of each feature map based on its contribution to the final reconstruction:

$$\begin{aligned} W_1 &= \text{MLP}(\text{Stack}(F_1)) \\ W_2 &= \text{MLP}(\text{Stack}(F_2)) \end{aligned} \quad (3)$$

Finally, the output of the VEMM is obtained by performing an element-wise multiplication of the features with their corresponding adaptive weights and concatenating the results:

$$\text{Out} = \text{Concat}(W_1 \odot F_1, W_2 \odot F_2) \quad (4)$$

This adaptive weighting mechanism empowers the model to dynamically emphasize features from the most informative scanning paths based on the input context.

3.4. Momentum Contrastive Learning

To enhance the model’s robustness and ensure a more faithful reconstruction of lateral information, we introduce an

Table 1. Quantitative evaluation of VEMamba. Comparison of VEMamba and Baseline (interpolation), IsoVEM, and EMDiffuse on the EPFL and CREMI datasets, using PSNR, SSIM, and LPIPS. The table also includes a comparison of computational cost and parameter count. The best results are highlighted in red, and the second-best results are in blue.

Method	Metrics	EPFL Dataset			CREMI Dataset			Flops(T) Params(M)
		×4	×8	×10	×4	×8	×10	
Baseline	PSNR	28.407	25.558	24.583	34.219	28.129	26.554	-
	SSIM	0.7478	0.6323	0.5891	0.9133	0.7861	0.7379	-
	LPIPS	0.2709	0.3955	0.4398	0.2811	0.4445	0.5031	-
IsoVEM	PSNR	29.234	27.119	26.138	37.807	31.449	29.662	0.61
	SSIM	0.7703	0.6839	0.6504	0.9485	0.8647	0.8296	1.40
	LPIPS	0.2196	0.3192	0.3546	0.2089	0.3208	0.3618	-
EMDiffuse	PSNR	27.522	24.947	24.407	36.305	29.027	27.131	22.51
	SSIM	0.6679	0.5733	0.5508	0.9326	0.7955	0.7214	15.16
	LPIPS	0.3716	0.4938	0.4596	0.1362	0.2418	0.3004	-
Ours	PSNR	29.422	27.418	26.473	37.785	31.556	29.796	0.28
	SSIM	0.7707	0.6816	0.6487	0.9869	0.9498	0.9278	0.94
	LPIPS	0.2176	0.3006	0.3388	0.2021	0.3129	0.3523	-

unsupervised strategy to learn and inject degradation representations into our network.

Degradation Representation Learning: Our objective is to learn a latent representation of the degradation information in an unsupervised manner. Specifically, we create a positive pair by sampling two subvolumes along its axial dimension. Subvolumes from different parent volumes form negative pairs. This process trains an encoder to capture implicit degradation features, optimized by the InfoNCE [5] loss. Given a batch of N volumes, each representing a unique degradation profile. From each volume i , we extract two subvolumes and encode them into a query q_i and a positive key k_{i+} . The remaining $N - 1$ keys from other volumes serve as negative samples. The training objective is thus as follows:

$$\mathcal{L}_D = - \sum_{i=1}^N \log \frac{\exp(q_i \cdot k_{i+} / \tau)}{\exp(q_i \cdot k_{i+} / \tau) + \sum_{\substack{j=1 \\ j \neq i}}^N \exp(q_i \cdot k_{j-} / \tau)} \quad (5)$$

where τ is a temperature hyper-parameter.

VDIM: Upon learning the degradation representation D , we integrate this information into our main reconstruction network. The VDIM adaptively modulates the network’s features by applying channel-wise affine transformations:

$$F' = \text{Linear}(D) \odot \text{Norm}(F) + \text{Linear}(D) \quad (6)$$

Here, F and F' represent the input and output feature, respectively.

By modeling and injecting this degradation-aware prior knowledge into the reconstruction network, our framework can perform a more targeted and precise restoration.

4. Experiments

4.1. Experimental settings

Implementation Details. Our proposed VEMamba was implemented in PyTorch and trained on two NVIDIA RTX 4090 GPUs. We employed the Adam [20] optimizer with a learning rate of 5×10^{-5} , which was adjusted by a cosine annealing scheduler following a 10 epoch warmup period. The model typically converged after 200 epochs. For training, we used a batch size of 2. The input subvolume dimensions were set to (32,128,128) for a scale factor of $\times 4$, (16,128,128) for $\times 8$, and (16,160,160) for $\times 10$. Our baseline model consists of 4 stacked RVMG blocks, with each RVMG block containing 4 RVMBs. The specific parameters for the degradation process (including blur, downsampling, and noise) follow the settings used in DiffuseEM [21].

Datasets. We validated our method on both isotropic and anisotropic datasets. For the isotropic dataset, we used the EPFL dataset [2], which contains a $5 \times 5 \times 5 \mu\text{m}^3$ volume of neural tissue from the hippocampal CA1 region acquired via FIB-SEM at a high resolution of $5 \times 5 \times 5 \text{ nm}^3/\text{voxel}$. To evaluate isotropic reconstruction, we synthetically generated anisotropic data by applying $\times 4$, $\times 8$, and $\times 10$ degradations along the z-axis. The CREMI dataset [7] consists of serial section TEM images of an adult *Drosophila melanogaster* brain. This dataset comprises three samples (A, B, and C), each with 193 sections at a resolution of $4 \times 4 \times 40 \text{ nm}^3/\text{voxel}$. Due to the sparse axial sampling, we conducted training and evaluation on the lateral planes for this dataset.

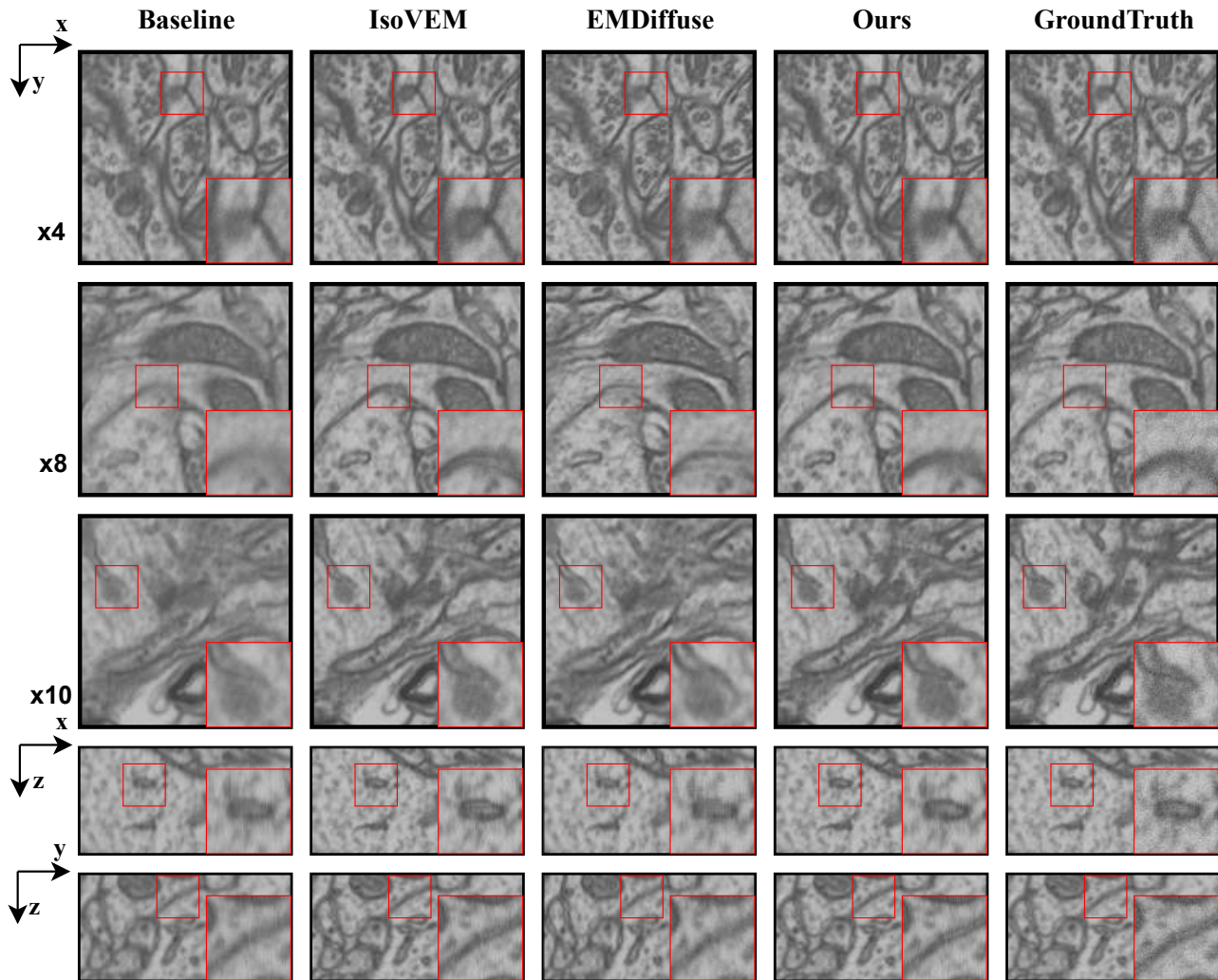


Figure 4. Qualitative comparison of baseline (Interpolation), IsoVEM, EMDiffuse, VEMamba, and Ground Truth on the EPFL dataset at scale factors of $\times 4$, $\times 8$, and $\times 10$ in the lateral (xy) and axial (xz and yz) section.

4.2. Experimental Results

To ensure a fair and rigorous comparison, we retrained IsoVEM and EMDiffuse on our experimental datasets, as their original publications either did not report metrics on these specific datasets or used different datasets. VEMamba demonstrates robust and highly competitive performance across both the EPFL and CREMI datasets.

Quantitative Comparison. The comprehensive quantitative results are presented in Table 1. In terms of PSNR, VEMamba achieves the top result in five out of six experimental settings. In these cases, it surpasses the second-best method by a significant margin of approximately 0.2-0.3 dB. In the single instance where our model ranked second, the performance gap was merely 0.022 dB, underscoring its consistent and robust performance. Similarly, for the SSIM,

VEMamba achieves the best results in four of the six experiments, again outperforming competitors by a substantial margin. For the two settings where it was the runner-up, the differences were minimal, at just 0.0023 and 0.0017, respectively. This highlights our model’s superior capability in preserving structural details during reconstruction. Furthermore, VEMamba shows highly competitive results on the LPIPS metric. Although it achieves the top score in three settings, it is worth noting that the LPIPS metric is pre-trained on RGB natural images. Its direct application to grayscale electron microscopy images may introduce a slight domain bias. Nevertheless, the strong performance indicates that our reconstructions are perceptually closer to the ground truth.

Qualitative Comparison. Visual comparisons provide further evidence of VEMamba’s superiority, as illustrated

	Baseline	IsoVEM	EMDiffuse	Ours	GroundTruth
x8	PSNR: 28.936 SSIM: 0.7687	PSNR: 31.408 SSIM: 0.8674	PSNR: 28.377 SSIM: 0.7836	PSNR: 31.834 SSIM: 0.9385	PSNR SSIM
x10	PSNR: 26.452 SSIM: 0.7238	PSNR: 29.042 SSIM: 0.8257	PSNR: 27.218 SSIM: 0.7208	PSNR: 29.742 SSIM: 0.9207	PSNR SSIM

Figure 5. Visual comparison of baseline (Interpolation), IsoVEM, EMDiffuse, VEMamba, and Ground Truth on the CREMI dataset at scale factors of $\times 8$ and $\times 10$ in the lateral (xy) section.

in Figure 4 for the lateral (xy) plane and the axial (xz and yz) planes. In the xy-plane reconstructions at a 4x scale factor, IsoVEM tends to hallucinate non-existent boundaries and textural details when compared to the GT. On the other hand, EMDiffuse struggles with reconstruction fidelity, failing to restore fine tissue structures accurately. In stark contrast, our model’s output is most faithful to the GT. This trend persists at higher magnification factors. At 8x, IsoVEM generates spurious membrane structures, while EMDiffuse fails to reconstruct them at all. VEMamba delivers the most accurate result. At the 10x scale, both IsoVEM and EMDiffuse are unable to produce complete and coherent tissue boundaries, whereas our method reconstructs them with remarkable clarity and integrity. The qualitative results in the xz and yz planes mirror these findings. Notably, in the xz-plane, IsoVEM produces prominent artifacts, which are particularly detrimental to achieving true isotropic reconstruction. The visualization results on the CREMI dataset are similar to those described above, as illustrated in Figure 5. Across all visual comparisons, VEMamba consistently yields the highest-quality reconstructions, free from the artifacts and structural inconsistencies that plague other methods. These qualitative results further validate the efficacy of our designed modules in implementing the proposed 3D dependency reordering.

Computational Cost. As detailed in Table 1, VEMamba is not only effective but also highly efficient. Our model features the lowest parameter count and computational load among all compared deep learning models. This combination of superior quantitative and qualitative performance with minimal resource requirements demonstrates the effi-

cacy and efficiency of our design. The lightweight nature of VEMamba facilitates easier deployment in real-world scenarios, offering a practical solution to enhance the imaging capabilities of volume electron microscopes and thereby advancing biomedical research.

4.3. Downstream Task

To assess the practical utility of our reconstruction, we evaluate its performance on a critical downstream task: mitochondria segmentation. High-quality isotropic reconstruction should not only exhibit high visual quality but also improve the accuracy of subsequent quantitative analyses, such as organelle segmentation, which is vital for biological studies. We employ a U-Net [28] architecture for segmentation, utilizing the Intersection over Union (IoU) as the primary evaluation metric. The network is trained for 200 epochs with the Adam optimizer, a learning rate of 1×10^{-4} , and the BCEWithLogitsLoss function.

As presented in Table 2, our proposed VEMamba consistently achieves state-of-the-art performance across all scale factors ($\times 4$, $\times 8$, and $\times 10$). Notably, the performance gap between our reconstruction and the isotropic ground truth is remarkably narrow, with an IoU difference of merely 0.002.

Qualitative comparisons, shown in Figure 7, corroborate these quantitative findings. The segmentations derived from our method’s output exhibit minimal noise and superior structural integrity. Compared to the baseline and other methods, our approach ensures the completeness of the mitochondria, with significantly fewer false negatives and discontinuities.

Table 2. Quantitative results of mitochondria segmentation (IoU) on the EPFL dataset. Our method achieves the best performance across all scale factors.

Metrics	EPFL Dataset			
	IoU	$\times 4$	$\times 8$	$\times 10$
Baseline	0.6889	0.6111	0.6099	
IsoVEM	0.7351	0.6834	0.6802	
EMDiffuse	0.7057	0.6197	0.6151	
Ours	0.7464	0.6975	0.6927	
Isotropic		0.7496		

Table 3. Ablation study of the proposed ALCSSM, DWAM, and MoCo modules on the EPFL dataset at a scale factor of $\times 4$, evaluated by PSNR and SSIM metrics.

ALCSSM	DWAM	MoCo	Metrics	
			PSNR	SSIM
✓		✓	29.381	0.7695
	✓	✓	29.372	0.7684
✓	✓		29.396	0.7699
✓	✓	✓	29.442	0.7707

4.4. Ablation Study

To validate the efficacy of our key designs, we performed comprehensive ablation studies on the EPFL dataset for $\times 4$ reconstruction. We systematically evaluate the contribution of each core component: the Axial-Lateral Chunking Selective Scan Modul (ALCSSM), the Dynamic Weights Aggregation Module (DWAM), and the Momentum Contrast based degradation learning.

As shown in Table 3, each component contributes to the final performance. Replacing our ALCSSM with a baseline continuous scan results in a 0.07 dB PSNR drop. Substituting our DWAM with simple feature summation causes a 0.061 dB decrease. Furthermore, removing the MoCo-based degradation learning leads to a 0.046 dB decline. Collectively, these results affirm that each proposed component contributes to the final state-of-the-art performance.

This is further supported by the qualitative analysis in Figure 6, which plots the axial pixel error. Our full model (“Ours”) maintains a minimal and stable deviation from the Ground Truth (0 line). In contrast, models lacking ALCSSM, DWAM or MoCo exhibit significant and erratic pixel differences, with large, fluctuating deviations from the ground truth. This visually confirms that ALCSSM, DWAM and MoCo are essential for establishing the robust axial-lateral consistency that our method promises.

5. Conclusion

In this work, we presented VEMamba, a self-supervised framework that pioneers the Mamba architecture for ef-

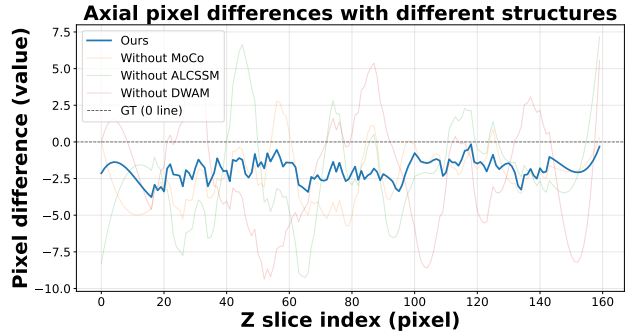


Figure 6. Visualization comparing the distances from GT along the Z-axis for different model architectures on the EPFL dataset.

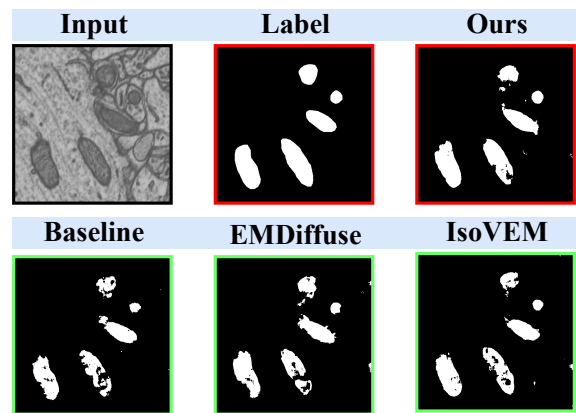


Figure 7. Visual comparison of mitochondria segmentation on the EPFL dataset.

ficient and effective VEM isotropic reconstruction. Our core innovations are the Axial-Lateral Chunking Selective Scan Module (ALCSSM), which establishes robust 3D axial-lateral consistency, and the Dynamic Weights Aggregation Module (DWAM), which adaptively fuses multi-directional representations. These two modules jointly realize 3D dependency reordering, ensuring globally consistent volumetric reconstruction. We further proposed a realistic degradation simulation strategy, leveraging MoCo to inject degradation-aware knowledge into the network. Extensive experiments demonstrated that VEMamba achieves highly competitive performance, surpassing existing methods in the majority of quantitative metrics, qualitative visual fidelity, and downstream segmentation tasks. Critically, VEMamba accomplishes this with significantly greater computational efficiency, requiring fewer parameters and a lower computational budget than competing models.

Acknowledgement

This work was supported by the Natural Science Foundation of China (No. 62272227).

References

- [1] Veronica Baena and Mark Terasaki. Three-dimensional organization of transzonal projections and other cytoplasmic extensions in the mouse ovarian follicle. *Scientific Reports*, 9:1262, 2019. 1
- [2] EPFL CVLab. Electron microscopy dataset, 2021. 5
- [3] B. D. de Senneville, F. Z. Khoubai, M. Bevilacqua, and et al. Deciphering tumour tissue organization by 3d electron microscopy and machine learning. *Communications Biology*, 4:1390, 2021. 1
- [4] Shiyu Deng, Xueyang Fu, Zhiwei Xiong, Chang Chen, Dong Liu, Xuejin Chen, Qing Ling, and Feng Wu. Isotropic Reconstruction of 3D EM Images with Unsupervised Degradation Learning. In *Medical Image Computing and Computer Assisted Intervention – MICCAI 2020*, pages 163–173. Springer International Publishing, Cham, 2020. Series Title: Lecture Notes in Computer Science. 2
- [5] Chris Dyer. Notes on noise contrastive estimation and negative sampling. In *arXiv preprint arXiv:1410.8251*, 2014. 5
- [6] Fisseha A. Ferede, Ali Khalighifar, Jaison John, Krishnan Venkataraman, and Khaled Khairy. Z-upscaling: Optical Flow Guided Frame Interpolation for Isotropic Reconstruction of 3D EM Volumes, 2024. arXiv:2410.07043 [eess]. 2
- [7] J. Funke and S. Saalfeld. Creml dataset, 2016. 5
- [8] Albert Gu and Tri Dao. Mamba: Linear-time sequence modeling with selective state spaces. In *arXiv preprint arXiv:2312.00752*, 2024. 2
- [9] Albert Gu, Isys Johnson, Karan Goel, Khaled Saab, Tri Dao, Atri Rudra, and Christopher Re. Combining recurrent, convolutional, and continuous-time models with linear state-space layers. In *arXiv preprint arXiv:2110.13985*, 2021. 2
- [10] Albert Gu, Karan Goel, and Christopher Re. Efficiently modeling long sequences with structured state spaces. In *arXiv preprint arXiv:2111.00396*, 2022. 2
- [11] Hang Guo, Jinmin Li, Tao Dai, Zhihao Ouyang, Xudong Ren, and Shu-Tao Xia. MambaR: A Simple Baseline for Image Restoration with State-Space Model, 2024. arXiv:2402.15648 [cs]. 2
- [12] Ken Hagita, Takashi Higuchi, and Hirofumi Jinnai. Super-resolution for asymmetric resolution of fib-sem 3d imaging using ai with deep learning. *Scientific Reports*, 8(1):5877, 2018. 2
- [13] Kenneth J. Hayworth, C. Shan Xu, Zhiyuan Lu, et al. Ultrastructurally smooth thick partitioning and volume stitching for large-scale connectomics. *Nature Methods*, 12(4):319–322, 2015. 2
- [14] Haoyang He, Jiangning Zhang, Yuxuan Cai, Hongxu Chen, Xiaobin Hu, Zhenye Gan, Yabiao Wang, Chengjie Wang, Yunsheng Wu, and Lei Xie. MobileMamba: Lightweight Multi-Receptive Visual Mamba Network, 2024. arXiv:2411.15941 [cs]. 4
- [15] Jia He, Yan Zhang, Wenhao Sun, Ge Yang, and Fei Sun. IsoVem: Isotropic reconstruction for volume electron microscopy based on transformer. *bioRxiv*, 2023. 2
- [16] Kaiming He, Haoqi Fan, Yuxin Wu, Saining Xie, and Ross Girshick. Momentum contrast for unsupervised visual representation learning. In *Proceedings of the IEEE/CVF Conference on Computer Vision and Pattern Recognition (CVPR)*, pages 9729–9738, 2020. 2
- [17] Larissa Heinrich, John A. Bogovic, and Stephan Saalfeld. Deep learning for isotropic super-resolution from non-isotropic 3d electron microscopy. In *Medical Image Computing and Computer-Assisted Intervention - MICCAI 2017*, pages 135–143, Cham, 2017. Springer International Publishing. 2
- [18] Brett E. Johnson and et al. An omic and multidimensional spatial atlas from serial biopsies of an evolving metastatic breast cancer. *Cell Reports Medicine*, 3(2):100525, 2022. 1
- [19] Mohammad Khateri, Morteza Ghahremani, Alejandra Sierra, and Jussi Tohka. Self-Supervised Super-Resolution Approach for Isotropic Reconstruction of 3D Electron Microscopy Images from Anisotropic Acquisition, 2023. arXiv:2309.10646 [eess]. 2
- [20] Diederik P. Kingma and Jimmy Ba. Adam: A method for stochastic optimization. In *arXiv preprint arXiv:1412.6980*, 2017. 5
- [21] Kyungryun Lee and Won-Ki Jeong. Reference-Free Isotropic 3D EM Reconstruction using Diffusion Models, 2023. arXiv:2308.01594 [cs]. 2, 5
- [22] Yu-Cheng Lin, Yu-Syuan Xu, Hao-Wei Chen, Hsien-Kai Kuo, and Chun-Yi Lee. EAMamba: Efficient All-Around Vision State Space Model for Image Restoration, 2025. arXiv:2506.22246 [cs]. 2
- [23] Chixiang Lu, Kai Chen, Heng Qiu, Xiaojun Chen, Gu Chen, Xiaojuan Qi, and Haibo Jiang. Diffusion-based deep learning method for augmenting ultrastructural imaging and volume electron microscopy. *Nature Communications*, 15(1):4677, 2024. 2
- [24] Shawn Mikula. Progress towards mammalian whole-brain cellular connectomics. *Frontiers in Neuroanatomy*, 10:62, 2016. 1
- [25] Josh L. Morgan and Jeff W. Lichtman. An individual interneuron participates in many kinds of inhibition and innervates much of the mouse visual thalamus. *Neuron*, 106(3):468–481.e2, 2020. 1
- [26] Masaaki Nagai and et al. Glomerular cellular interactions following disruption of the glomerular basement membrane in iga nephropathy: Ultrastructural analyses by 3-dimensional serial block-face scanning electron microscopy. *Kidney Medicine*, 2(2):222–225, 2020. 1
- [27] Mingjie Pan, Yulu Gan, Fangxu Zhou, Jiaming Liu, Aimin Wang, Shanghang Zhang, and Dawei Li. DiffuseIR: Diffusion Models For Isotropic Reconstruction of 3D Microscopic Images, 2023. arXiv:2306.12109 [eess]. 2
- [28] Olaf Ronneberger, Philipp Fischer, and Thomas Brox. U-net: Convolutional networks for biomedical image segmentation. In *arXiv preprint arXiv:1505.04597*, 2015. 7
- [29] Kerriane Ryan and et al. The cns connectome of a tadpole larva of *Ciona intestinalis* (L.) highlights sidedness in the brain of a chordate sibling. *eLife*, 5:e16962, 2016. 1
- [30] Shijun Shi, Jing Xu, Lijing Lu, Zhihang Li, and Kai Hu. Self-supervised ControlNet with Spatio-Temporal Mamba for Real-world Video Super-resolution, 2025. arXiv:2506.01037 [cs]. 4

- [31] Amelia Shoemark and et al. Primary ciliary dyskinesia with normal ultrastructure: three-dimensional tomography detects absence of dnaH11. *The European Respiratory Journal*, 51(2):1701809, 2018. [1](#)
- [32] Amelia Shoemark and et al. International consensus guideline for reporting transmission electron microscopy results in the diagnosis of primary ciliary dyskinesia (beat ped tem criteria). *The European Respiratory Journal*, 55(4):1900725, 2020. [1](#)
- [33] Jimmy Smith, Andrew Warrington, and Scott W. Linderman. Simplified state space layers for sequence modeling. *ArXiv*, abs/2208.04933, 2022. [2](#)
- [34] Takashi Takaki and et al. Podocyte penetration of the glomerular basement membrane to contact on the mesangial cell at the lesion of mesangial interposition in lupus nephritis: a three-dimensional analysis by serial block-face scanning electron microscopy. *Clinical and Experimental Nephrology*, 23(6):773–781, 2019. [1](#)
- [35] Mark et al. Terasaki. Stacked endoplasmic reticulum sheets are connected by helicoidal membrane motifs. *Cell*, 154(2):285–296, 2013. [1](#)
- [36] Ashish Vaswani, Noam Shazeer, Niki Parmar, Jakob Uszkoreit, Llion Jones, Aidan N Gomez, Lukasz Kaiser, and Illia Polosukhin. Attention is all you need. *arXiv*, 2017. [2](#)
- [37] Wenhai Wang, Enze Xie, Xiang Li, Deng-Ping Fan, Kaitao Song, Ding Liang, Tong Lu, Ping Luo, and Ling Shao. Pvt v2: Improved baselines with pyramid vision transformer. *Computational Visual Media*, 8(3):415–424, 2022. [3](#)
- [38] Zejin Wang, Guodong Sun, Lina Zhang, Guoqing Li, and Hua Han. Temporal Spatial-Adaptive Interpolation with Deformable Refinement for Electron Microscopic Images, 2021. *arXiv:2101.06771 [cs]*. [2](#)
- [39] Courtney E. Wilson and et al. Taste bud connectome: Implications for taste information processing. *The Journal of Neuroscience*, 42(5):804–816, 2022. [1](#)
- [40] Pang S. Shtengel G. et al. Xu, C.S. An open-access volume electron microscopy atlas of whole cells and tissues. *Nature*, 599(7883):147–151, 2021. [1](#)
- [41] Pang S. Shtengel G. et al. Xu, C.S. Publisher correction: An open-access volume electron microscopy atlas of whole cells and tissues. *Nature*, 599(7885):E5, 2021. [1](#)